Modeling of an Energy Harvesting Hybrid Radio Frequency Optical Wireless Sensor Network

ALEXANDROS ASLANIDIS[1*], THOMAS KAMALAKIS[1], STANISLAV ZVANOVEC[2], RAUL ZAMORANO-ILLANES[3], AND ZABIH GHASSEMLOOY[3]

[1] Department of Informatics and Telematics, Harokopio University of Athens, Athens, Greece
[2] Department of Electromagnetic Fields, Faculty of Electrical Engineering, Czech Technical University in Prague, Prague, Czech Republic
[3] Optical Communication Research Group, Faculty of Engineering and Environment, Northumbria University, Newcastle upon Tyne, UK
[*] aaslan@hua.gr

Compiled February 19, 2026

Sixth generation (6G) wireless sensor networks with energy harvesting will foster the creation of smart environments that prioritize efficiency, safety, and user-centric functionality while enabling scalable, sustainable, and autonomous networking. This paper presents a hybrid architecture that leverages visible light communication and radio-frequency transceivers for the downlink and uplink respectively, providing seamless wireless connectivity. This approach not only alleviates radio spectrum congestion by offloading data traffic to the optical channel, but also improves energy efficiency by re-using illumination light for communication purposes. We provide an open-source `Python` module capable of simulating key aspects, including the physical and medium access control layers as well as energy harvesting. Our results demonstrate the feasibility of self-sustaining wireless sensor nodes for a wide range of indoor scenarios, aligning with the 6G objectives of energy-efficient, low-powered, and environmentally sustainable systems.

http://dx.doi.org/10.1364/ao.XX.XXXXXX

1. INTRODUCTION

Sixth generation (6G) technology is expected to support a range of internet-of-things (IoT) applications, from autonomous healthcare to smart cities and beyond [1]. Wireless sensor networks (WSNs) [2] are pivotal in enabling various applications by leveraging their ability to collect, transmit, and analyze environments. Meanwhile, energy harvesting (EH) schemes [3] are considered important ingredients for achieving energy efficiency and self-sustainability in 6G. However, the massive number of connected devices and applications will lead to further congestion of the radio frequency (RF) spectrum, making it necessary to utilize new frequency bands. Visible light communications (VLC) is a potential alternative wireless technology, which uses light emitting diodes (LEDs)-based light fixtures for simultaneous illumination, data communications, and positioning. Taking advantage of the widespread presence of LED-based lighting infrastructure, it offers vast bandwidth availability, immunity to the RF-induced interference and inherently secure communication at the physical layer [4]. IoT-related VLC use cases have already emerged in various areas, including wireless body area networks (WBAN) [5], industrial IoT [6], smart agriculture [7] and vehicle-to-vehicle (V2V) communication [8]. In indoor environments, VLC is primarily used for the downlink, while the uplink may rely on infrared (IR) or RF. Use cases for IoT VLC systems are discussed in [9].

High speed, hybrid VLC/RF systems are actively being researched for wireless local area networks (WLANs) [10], but these are generally unsuitable for IoT use cases due to increased power consumption. In this paper, we instead consider an energy harvesting hybrid optical wireless RF (EH-OWRF) approach, especially suited for sustainable WSNs. Figures 1a and 1b show the sensor node (SN) architecture and the proposed WSN scenario used in our work. RF is solely used for the uplink to send data from the SN to a master node (MN), which sends back acknowledgments (ACKs) through the VLC downlink. Offloading some of the traffic to the optical channel alleviates RF spectrum congestion. The VLC downlink reuses illumination LEDs to simultaneously transmit data, thereby enhancing energy efficiency. Energy harvesting (EH) is achieved using photovoltaic (PV) panels at the SNs. In our scenarios, we consider rather large (e.g. $10 \times 10 \times 3$ m^3) rooms with windows, typical of hospital, warehouse, university, and industrial environments, where WSNs could be used for healthcare monitoring, security/surveillance, asset tracking and smart building management [11]. Our approach is easily extendable to smaller rooms in domestic environments as well.

We contribute to the existing state-of-the-art, first, by developing a full-blown hybrid WSN simulator incorporating all system aspects, such as the optical/RF transceivers and channels, including line of sight (LOS) and non-LOS components, the medium

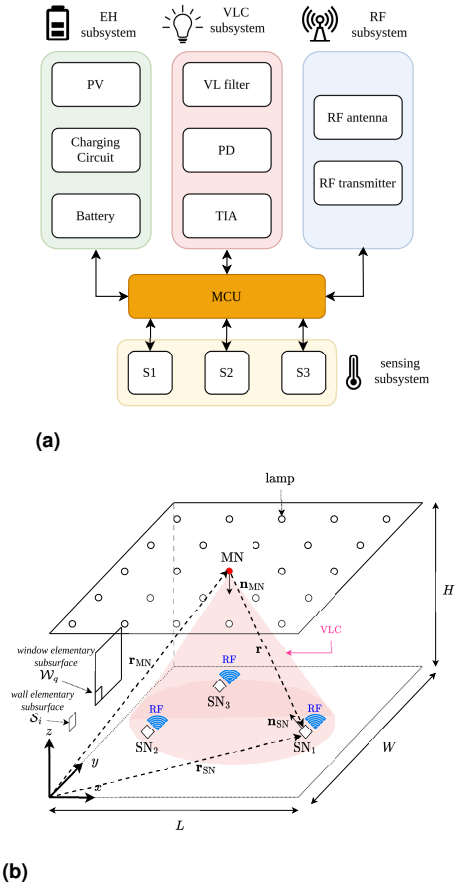

Fig. 1. (a) SN subsystems: PV→photovoltaic panel, VL→visible light filter, TIA→transimpendance amplifier, MCU→ microcontroller unit. S1, S2 and S3 represent the sensors attached. (b) Proposed system architecture where SNs send data to the MN via RF links and receive ACKs via VLC.

access control (MAC) protocol, battery charging circuits, and PV panels. Realistic models based on IEEE 802.15.4 are considered for the RF channel, while we implement an unslotted carrier sense multiple access with collision avoidance (CSMA/CA) simulator for the MAC layer. Our WSN model includes a detailed energy consumption model and an accurate 5-parameter model of the SN PV panels. We consider three representative scenarios, characterized by varying levels of sunlight interference. We also assess system performance in the diffuse regime to ascertain system robustness under temporary or permanent LOS blockage due to obstacles. We account for shadowing effects in the RF channel and propose a rigorous approach for estimating harvested energy that considers PV panel characteristics and light propagation in an indoor environment. To the best of our knowledge, no previous work has addressed all these aspects in such a unified and detailed manner. Our `Python`-based simulator is publicly available as open-source [12], enabling researchers to alter scenario parameters and component specifications to meet their particular requirements. Applying this tool, we demonstrate several aspects of the EH-OWRF system for the first time in the literature. Specifically, we show that: (i) under normal sunlight, only 30–60 minutes of daily EH using a commercial PV panel is sufficient to achieve a zero-energy deficit at most sensor node (SN) locations; (ii) in the absence of sunlight, we identify the requirements needed to sustain optimal EH from ceiling lamps during an 8-hour daily harvesting period; (iii) diffuse light alone can maintain adequate downlink performance when the LOS is blocked; and (iv) the hybrid approach performs well in terms of energy efficiency, thanks to the lower power consumption of optical receivers at the SNs and the enhanced MAC protocol. Our results show that EH-RFOW is a viable solution for low-energy 6G WSNs, significantly enhancing self-sustainability in indoor environments. Since we use realistic system models, we expect an agreement with practical implementations.

Pertinent literature includes [13], which adopts VLC/RF for communication and positioning applications in the mining industry, and briefly addresses energy consumption using rather simplistic models for VLC/RF channels. Simultaneous lightwave information and power transfer (SLIPT) is introduced in [14], which analyzes the tradeoffs between quality-of-service (QoS) and EH when a PV panel is also used for data reception using simplified EH models, and without accounting for the relationship between irradiance and PV efficiency. Resource allocation and dual-hop relay selection for EH-RFOW systems are studied in [15] and [16], respectively. In [17], a resource allocation algorithm is studied to maximize aggregate uplink / downlink data rates for a hybrid system with EH capabilities. In [18], a hybrid EH-enabled light fidelity / wireless fidelity (LiFi/WiFi) system is presented, but power consumption and EH are not investigated. Outage probability expressions are derived for a hybrid system in [19], assuming photodiodes (PDs) are used for both data communication, imposing low duty cycle signaling to offset the inefficient EH with PDs.

The rest of the paper is organized as follows: Section 2 presents the detailed EH-OWRF system and the models for its various subsystems. Section 3 provides the basic approach for estimating energy consumption and harvesting. In this section, we also calculate the SN lifetime, as well as the optimal PV panel placement to maintain zero energy deficit operation. The concluding remarks are then given in Section 4.

2. HYBRID SYSTEM DESCRIPTION

The SN, shown in Figure 1, includes a microcontroller unit (MCU) and four subsystems, namely the EH with battery, charging, and PV modules; VLC, which includes a visible light (VL) filter, PD and transimpedance amplifier (TIA); RF, with transmitter and antenna modules; and sensing. Although PV panels can also serve as optical receivers [16], we have chosen to use PDs instead, to simplify the receiver design and improve the performance of the system. The MCU coordinates the functions of the nodes and puts them in standby mode following successful transmission. Similarly, the MN comprises an LED lamp and its driver, an optical transmitter, an RF receiver and its MCU. We further describe the subsystems in the following subsections. The key system and scenario parameters are outlined in Table 1.

A. VLC downlink

At the MN, the ACK signal is used for intensity modulation of the LED via the driver circuit. Assuming that the transmitter follows a Lambertian order m, the LOS gain is given by [20]:

$$h = h(\mathbf{r}_S, \mathbf{r}_R) = \frac{m+1}{2\pi R^2} A_{\text{eff}} \text{rect}\left(\frac{\theta}{\text{FOV}}\right) \cos^m \phi \cos\theta \qquad (1)$$

with $R = |\mathbf{r}|$, where $\mathbf{r} = \mathbf{r}_S - \mathbf{r}_R$, being the distance between the transmitter (located at $\mathbf{r}_S$) and the receiver (located at $\mathbf{r}_R$), $\cos\theta = \mathbf{n}_R \cdot \mathbf{r}/R$, $\cos\phi = -\mathbf{n}_S \cdot \mathbf{r}/R$, A_{eff} and FOV are the receiver area and field-of-view, respectively, $\mathbf{n}_S$ and $\mathbf{n}_R$ are unity

Room characteristics	
Length (L) × width (W) × height (H)	10 m × 10 m × 3 m
Wall and ceiling reflectivity ($\mathcal{R}_w, \mathcal{R}_c$)	0.6
Floor reflectivity ($\mathcal{R}_f$)	0.3
Lighting LEDs	24
Window	
Size (scenario A)	2 m × 2 m
Size (scenario B)	8 m × 1 m
Spectral irradiance (p_n)	1.5 W/nm/m^2
Sunlight temperature (T_K)	5800 K
Diffuse VLC channel parameters	
Elementary subsurfaces per wall (N_E)	20
Master node (VLC)	
Position ($\mathbf{r}_{MN}$)	(5, 5, 3)
Orientation ($\mathbf{n}_{MN}$)	(0, 0, -1)
LED power (P_{MN})	6W
Pattern order (m)	1
Modulation	OOK
Spectral efficiency (e_{mod})	0.4 b/s/Hz
Bandwidth (B_e)	625 kHz
Bit-rate (R_d)	250 kbps
Sensor node (VLC)	
Field-of-view (FOV$_{SN}$)	$\pi/2$
Position ($\mathbf{r}_{SN}$)	$(x, y, 0)$
Orientation ($\mathbf{n}_{SN}$)	$(0, 0, 1)$
Responsivity	VTB5051BH [20]
Rejection filter	VTB5051BH [20]
TIA model	[20]
Detector area (A_{eff})	1 cm^2
RF subsystem	
Carrier frequency (f_c)	2.4 GHz [21]
Tx antenna gain (G_t)	0 dBi
Rx antenna gain (G_r)	0 dBi
Sensitivity (p_{sens})	-99 dBm [21]
Data rate (R_u)	250 kbps [21]
TX power (P_t)	Eq. (7)

RF channel [22]	
Reference distance (R_0)	2 m
Reference loss ($l_{RF}(R_0)$)	-50.7 dB
Loss coefficient (α)	2.6
Shadowing loss std (σ)	5.8 dB
SN current draw	
Sleep (I_{SL})	2 μA [21]
ADC (I_{ADC})	0.7 mA [21]
Wakeup (I_{WU})	1 mA [21]
Channel assessment (I_{CCA})	6.4 mA [21]
Active (I_{ACT})	2.73 mA [21]
TIA (I_{TIA})	0.7 mA
Sensing (I_{SENS})	Eq. (12)
Transmitting (I_{TX})	Eq. (13)
Receiving (I_{RX})	Eq. (14)
MQ2 gas sensor (I_1)	0.16 A
DHT11 temperature sensor (I_2)	0.2 mA
TSL2561 luminosity sensor (I_3)	0.5 mA
Timings	
MCU frequency (f_{MCU})	48 MHz [21]
Sampling frequency (f_S)	200 kHz [21]
Medium access control	
Min backoff exponential (e_{min})	3
Max backoff exponential (e_{max})	5
Max number of backoffs (n_{max})	5
Max backoff retransmissions (r_{max})	5
RF Packet length (L_p)	20 bytes
ACK Length (L_{ACK})	10 bytes
PV specifications [23]	
Reference irradiance (G_0)	1 $\frac{kW}{m^2}$
Open-circuit voltage (V_{oc})	2.79 V
Open-circuit current (I_{sc})	165 mA
Maximum power voltage (V_{mp})	2.24 V
Maximum power voltage (I_{mp})	140 mA
Area (A_{PV})	27 cm^2
Number of cells (N_{cell})	4

PV circuit parameters	
Photocurrent (I_{ph})	165 mA
Dark saturation current (I_0)	9.31 pA
Series resistance (R_s)	664 mΩ
Parallel resistance (R_p)	105.6 Ω
Ideality factor (n)	1.2
PV absorption model	
Absorption coefficient (α)	[24]
PV responsivity polynomial fitting	
a_7	$3.10974 \cdot 10^{-19}$ A/(Wnm^7)
a_6	$-1.43654 \cdot 10^{-15}$ A/(Wnm^6)
a_5	$2.70105 \cdot 10^{-12}$ A/(Wnm^5)
a_4	$-2.66571 \cdot 10^{-9}$ A/(Wnm^4)
a_3	$1.482177 \cdot 10^{-6}$ A/(Wnm^3)
a_2	$-4.622185 \cdot 10^{-4}$ A/(Wnm^2)
a_1	$7.611403 \cdot 10^{-2}$ A/(Wnm)
a_0	-5.181545 A/W
Battery and charging	
Supply Voltage (V_s)	3 V
Self-discharge current (I_{SD})	1 μA
Capacity (Q_{batt})	250 mAh
Max converter power (P_{bb})	294 mW
Converter efficiency (η_{bb})	80%
VLC worst case SNR	
Scenario A	26.7 dB
Scenario B	27.7 dB
Scenario C	40.9 dB
Scenario A (diffuse)	19.8 dB
Scenario B (diffuse)	20.3 dB
Scenario C (diffuse)	35.6 dB
Minimum energy harvesting	
Scenario A	2.6 J/h
Scenario B	15.6 J/h
Scenario C	0.45 J/h
Energy consumption	
Max consumption ($\mathcal{E}_{day,max}$)	7.55 J/day
Min node life ($T_{batt,min}$)	440 days

Table 1. Simulation parameters and indicative results

normal vectors, respectively describing the orientation of the transmitter and receiver while rect$(\cdot)$ is the rectangular function.

Assuming that $\mathbf{r}_{MN}$ and $\mathbf{r}_{SN}$ are the positions of the MN and SN, respectively (shown in Figure 1b), the LOS optical power, P_{LOS}, is calculated as: $P_{LOS} = h(\mathbf{r}_{MN}, \mathbf{r}_{SN})P_{LAMP}$, where P_{LAMP} is the transmit power of the VLC lamp. Additionally, in an indoor environment, there is a diffuse component P_D that arises from the multiple bounces of light on the surfaces of the room, which can be estimated following the approach of [25]. We assume that all surfaces of the room, including walls, ceiling, and floor, consist of elementary flat subsurfaces $\mathcal{S}_i$ located at $\mathbf{r} = \mathbf{r}_i$, with reflectivity $\mathcal{R}_i$. P_D is calculated as the sum of optical power at the receiver from multiple light bounces at $\mathcal{S}_i$. At the first bounce, we calculate the power $P_i^{(0)}$ received at every $\mathcal{S}_i$ from the light source. The power reflected back from $\mathcal{S}_i$ is equal to $\mathcal{R}_i P_i^{(0)}$ and we can use Eq. (1) to estimate the power $P_R^{(1)}$ at the SN and the incident power $P_i^{(1)}$ at every subsurface. We then proceed accordingly to calculate the contribution of the next bounce, and so forth. At the b^{th} bounce, the power incident on each subsurface is:

$$P_i^{(b)} = \sum_{q=1}^{N_E} h(\mathbf{r}_q, \mathbf{r}_i)\mathcal{R}_q P_q^{(b-1)} \quad \textbf{(2)}$$

where N_E is the number of elementary subsurfaces. The diffuse power component P_D at the SN is simply the sum of the power obtained at each bounce and from each subsurface, which is given by:

$$P_D = \sum_{b=1}^{N_B} \sum_{i=1}^{N_E} h(\mathbf{r}_i, \mathbf{r}_{SN})\mathcal{R}_i P_i^{(b)} \quad \textbf{(3)}$$

In our simulations, we consider $N_B = 4$ bounces, noting that contributions for $N_B \leq 2$ are the most critical, while those for $N_B > 4$ can be neglected [25]. We also need to consider the spectral properties of the transceivers. Following the approach of [20], the VLC transmitter spectrum $\mathcal{R}_S(\lambda)$, is approximated by the sum of two Gaussian functions, corresponding to the blue ($\lambda = 470$ nm, FWHM $= 20$ nm) and phosphor ($\lambda = 600$ nm, FWHM $= 100$ nm) components. The SN receiver is modeled based on the characteristics of a VTB5051BH silicon PD with a built-in IR rejection filter, with transfer function

$\mathcal{R}_{\mathrm{R}}(\lambda)$, which is described by a third-order super-Gaussian function with a 10 dB bandwidth of 230 nm, peaking at 435 nm. The responsivity $\mathcal{R}_{\mathrm{D}}(\lambda)$ of the PD is described by polynomial fitting the experimental data from the responsivity curve. The effective responsivity $\mathcal{R}_{\mathrm{eff}}$ is the overlap between these spectra, as given by:

$$\mathcal{R}_{\mathrm{eff}} = \int_0^{+\infty} \mathcal{R}_{\mathrm{D}}(\lambda)\mathcal{R}_{\mathrm{R}}(\lambda)\mathcal{R}_{\mathrm{S}}(\lambda)\mathrm{d}\lambda \quad \textbf{(4)}$$

and describes the ratio of the PD current to the incident optical power. Retracing the calculations in [20], $\mathcal{R}_{\mathrm{eff}}$ is determined to be ≈ 0.32 A/W. Assuming on/off keying (OOK),the signal-to-noise ratio (SNR) is defined as:

$$\mathrm{SNR} = \frac{1}{4}\frac{\mathcal{R}_{\mathrm{eff}}^2(P_{\mathrm{LOS}} + P_{\mathrm{D}})^2}{\sigma_{\mathrm{th}}^2 + \sigma_{\mathrm{sh}}^2} \quad \textbf{(5)}$$

where $\sigma_{\mathrm{sh}}^2 = 2qI_{\mathrm{amb}}B_{\mathrm{e}}$ is the shot noise power due to the power noise, q is the electron charge, B_{e} is the electrical bandwidth and I_{amb} is the ambient-light induced photocurrent, while σ_{th}^2 is the TIA thermal noise power. Note that $B_{\mathrm{e}} = R_{\mathrm{d}}/e_{\mathrm{mod}}$, where R_{d} is the data rate and e_{mod} is the spectral efficiency of OOK, which is assumed to be 0.4 b/s/Hz [20]. Note that all other noise sources are ignored since their contributions are too small compared to the thermal and ambient-induced shot noise sources. To calculate I_{amb}, we need to consider all ambient light sources in the room, including the windows and lamps. The windows are split into elementary subsurfaces $\mathcal{W}_q$ (each located at $\mathbf{r} = \mathbf{r}_q$). We obtain this ambient light current contribution as [20]:

$$I'_{\mathrm{amb}} = \sum_{q=1}^{N_{\mathrm{W}}} \mathcal{W}_q h(\mathbf{r}_q, \mathbf{r}_{\mathrm{SN}}) \int_0^{+\infty} s_q(\lambda)\mathcal{R}_{\mathrm{R}}(\lambda)\mathcal{R}_{\mathrm{D}}(\lambda)\mathrm{d}\lambda \quad \textbf{(6)}$$

where $s_q(\lambda)$ is the spectral irradiance of $\mathcal{W}_q$. In daylight conditions, we approximate the window irradiance using a blackbody radiation distribution at an absolute temperature of 5800 K and peak irradiance of 1.5 W/m^2/nm [26]. We can also determine the ceiling lamps' contribution to ambient noise, $I''_{\mathrm{amb}} = \mathcal{R}_{\mathrm{eff}}P''_{\mathrm{amb}}$, by estimating the corresponding optical power P''_{amb}, using the same approach we presented for the VLC transmitter. The total ambient light-induced current is $I_{\mathrm{amb}} = I'_{\mathrm{amb}} + I''_{\mathrm{amb}}$. The bit error ratio (BER) is estimated as $P_{\mathrm{e}} = Q(\sqrt{\mathrm{SNR}})$, where Q is Marcum Q-function [20].

In Figure 2, we show the SNR obtained for the room in Figure 1b assuming a width $W = 10$ m, a length $L = 10$ m, and a height $H = 3$ m, using Eq. 5. We consider three scenarios. In the first two, a 2×2 m^2 (scenario A) and a 8×1 m^2 window (scenario B) are located at the center of the western wall at $(0, W/2, H/2)$. In the third case (scenario C), there are no windows.

A uniform grid of 5×5 LED lamps is assumed at the ceiling, spanning from $x = y = 1$ m to $x = y = 9$ m, corresponding to ≈ 550 lux. The center lamp placed at $(W/2, H/2, L)$, serves as the VLC transmitter. The optical power of each lighting LED is 6 W and the order of the Lambertian pattern is $m = 1$. We assume a downlink R_{d} of 250 kbps and calculate the required B_{e} of 625 kHz. Also, note that (i) B_{e} is less than the bandwidth of a typical white LED [27], and (ii) in the sub-MHz range the diffuse channel gain can be considered flat [25]. The key parameters and results for the VLC simulations are shown in Table 1, which also includes some key findings from the following sections. In Figure 2c, we show the SNR calculated when only the ambient light noise due to the lighting lamps is considered (scenario C), while in Figures 2a, 2b we include the effect of sunlight, for scenarios A and B, respectively. The reflectivity $\mathcal{R}_i$ is assumed

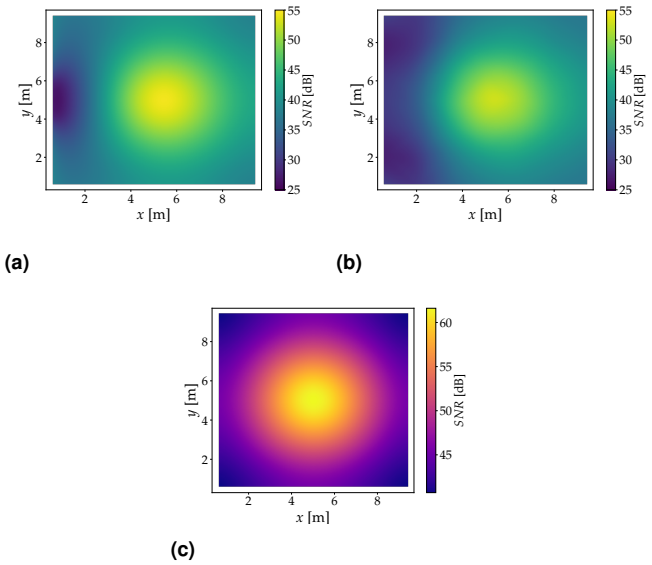

Fig. 2. SNR for the VLC link for: (a) scenario A, (b) scenario B, and (c) scenario C.

0.6 for the wall and ceiling surfaces (corresponding to white painted concrete) and 0.3 for the floor (corresponding to timber floor). The active area of the PD is $A_{\mathrm{eff}} = 1$ cm^2 while the FOV is assumed $\pi/2$. We vary the SN position along a 50×50 uniform grid at the floor level. Including the TIA noise as modeled in [20] and the ambient shot noise, we obtain an SNR larger than 26 dB in all positions, which practically guarantees error-free communication for the downlink (BER $< 10^{-6}$), well below the forward error correction limit of $3.8 \cdot 10^{-3}$ [27]. For scenarios A and B, the worst SNR is observed for SNs near the window due to the increased I'_{amb}, which reaches values up to 2 mA. In scenario C, the worst SNR occurs in the corners of the room, where the incident power from the MN is minimal, even though I''_{amb} is maximum at the center of the room, reaching up to 42 μA.

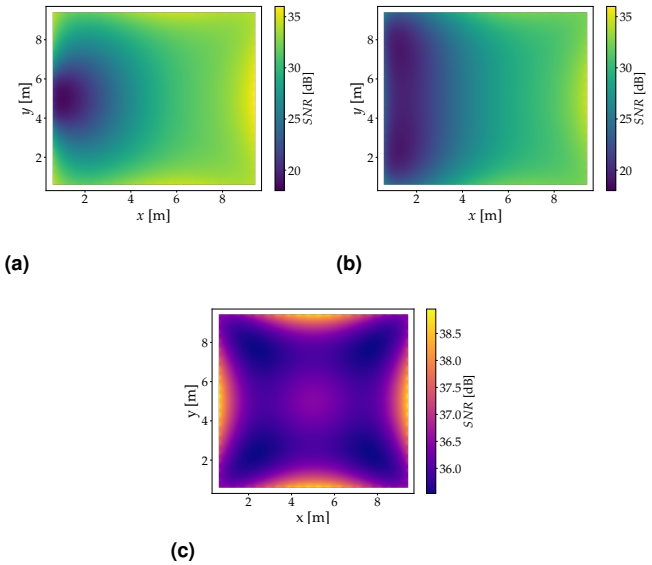

Fig. 3. SNR for the diffuse VLC link for (a) scenario A, (b) scenario B and (c) scenario C.

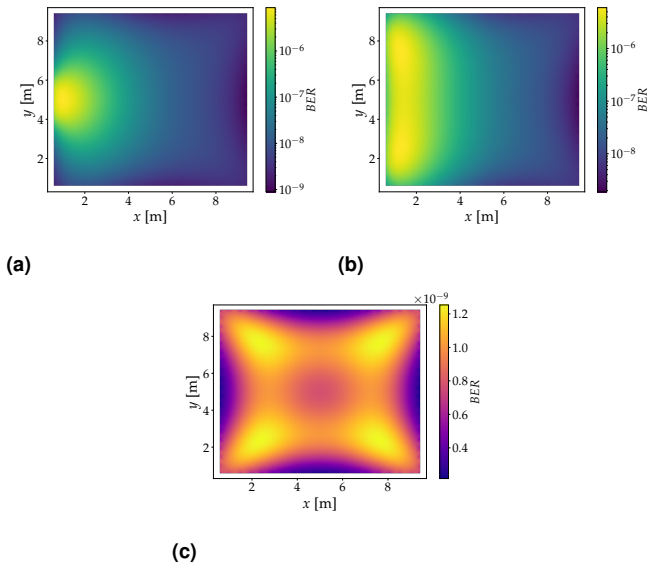

Fig. 4. BER for the diffuse VLC link for (a) scenario A, (b) scenario B and (c) scenario C.

To account for obstacles, we also estimate the SNR in the diffuse regime, assuming $P_{\text{LOS}} = 0$. Figure 3 illustrates the diffuse SNR profiles, which, as expected, are worse than those in Figure 2. In Figures 3a, 3b where sunlight is included, the SNR is degraded near the window. Compared to scenario A, an average degradation of ≈ 3 dB is observed for the SNR values in scenario B for both VLC links due to increased sunlight. However, it remains ≥ 19 dB across the floor level, which corresponds to BER $< 10^{-5}$ as shown in Figure 4, for all scenarios. As expected, the SNR is much better in the absence of sunlight, as shown in Figure 3c. In this case, higher SNR values are obtained near the walls, which act as secondary transmitters.

B. RF uplink

The log-normal shadowing model can be used to predict the path loss for the RF uplink, which is approximated by:

$$L_{\text{RF}}(R)\ [\text{dB}] = 10\alpha \log_{10}(R/R_0) + L_0(R_0) + X_{\text{sh}} \qquad (7)$$

where α, R_0 and $L_0(R_0)$ are empirical coefficients related to different sites and conditions, while X_{sh} is a Gaussian zero-mean random variable with standard deviation σ, which is due to shadowing. For simulation purposes, we use the values from [22] for the indoor scenario, as shown in Table 1. Taking into account the cumulative probability density function (CDF) of the normal distribution, $X_{\text{sh}} \geq -2.3\sigma$ with $> 99\%$ probability. In our calculations, we therefore assume $X_{\text{sh}} = 2.3\sigma$ to ensure at least 99% availability. The link budget is written as:

$$P_{\text{r}}(R) = P_{\text{t}} + G_{\text{t}} + G_{\text{r}} - L_{\text{RF}}(R) \qquad (8)$$

where P_{t} and P_{r} is the RF transmit and received power in dBm, respectively, while G_{t} and G_{r} is the transmitter and receiver antenna gains in dBi, respectively. We need $P_{\text{r}} > p_{\text{sens}}$, with p_{sens} being the RF receiver sensitivity. In our calculations, we assume p_{sens} =-99 dBm based on the SimpleLink CC1352P7 platform [21], obtained at a carrier frequency $f_{\text{c}} = 2.4$GHz, assuming offset quadrature phase-shift keying (OQPSK) modulation with 4 bits/symbol, a direct-sequence spread spectrum (DSSS) spreading factor of 1:8, and an effective bit rate $R_{\text{u}} = 250$ kbps, as proposed in [28]. Alternatively, we can obtain p_{sens} analytically [29]. For simplicity, the antenna gain for both the receiver and the transmitter is set to $G_{\text{t}} = G_{\text{r}}$ =0 dBi, which corresponds to ideal isotropic antennas. The simulation parameters for the RF transceiver model can also be found in Table 1. Figure 5 shows the minimum required RF transmit power and the corresponding current for SNs positioned at the floor diagonal $(x, x, 0)$. We observe that the power required varies significantly starting from ≈ -23 dBm at the center of the floor and reaching ≈ -15 dBm near its edges. In the sections that follow, we will use this approach to estimate the required RF transmit power.

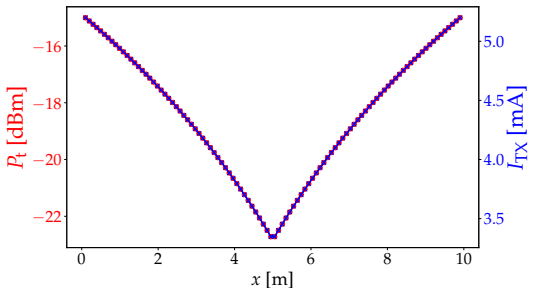

Fig. 5. Minimum required RF transmit power and the corresponding current consumption.

C. MAC layer

The MAC protocol used to coordinate the transmissions of multiple SNs is based on the IEEE 802.15.4 unslotted CSMA/CA protocol for single-hop star topologies [28]. The protocol introduces three variables, namely the backoff exponential, e_{b}, the number of backoffs n_{b}, and the number of frame retransmission attempts, r_{t}. The algorithm's performance is determined by the minimum and maximum value of the backoff exponential, e_{min} and e_{max}, respectively, and the maximum number of allowed backoff and retransmission attempts n_{max} and r_{max}, respectively. In our simulations, we let $n_{\text{max}} = 5$, $e_{\text{min}} = 3$, $e_{\text{max}} = 5$ and $r_{\text{max}} = 5$. We assume a backoff period T_{b} of 20 symbol durations, which, for the SN data rate of $R_{\text{u}} = 250$ kbps, corresponds to 16 μs, and that every SN attempts to transmit periodically with period T.

On idle intervals, the SN enters sleep mode to conserve energy. When it is about to transmit data, n_{b} and r_{t} are initialized to zero while e_{b} is set equal to e_{min}. Next, the SN awaits n backoff periods where n is an integer randomly selected inside the interval $I_{\text{b}} = [0, 2^{e_{\text{b}}})$. It then performs a clear channel assessment (CCA) to determine whether the channel is available to transmit. If the channel is busy, and $n_{\text{b}} < n_{\text{max}}$, then n_{b} is increased by 1. Otherwise, if $n_{\text{b}} \geq n_{\text{max}}$, failure is reported and transmission is aborted while e_{b} is increased by 1, provided it has not exceeded its maximum value e_{max} and the SN re-enters the backoff state. If the channel is free, then the data packet is transmitted. The MCU then powers on the optical receiver and waits for an ACK from the MN. If ACK is not received within a specified duration T_{max}, and if r_{t} has reached its maximum value r_{max}, the data packet is discarded; otherwise, r_{t} is increased by 1 and the transmission process starts again.

The process is illustrated in Figure 6. A discrete-event simulator implemented in `Python` is used to describe the behavior of the SN. The time resolution is set equal to one backoff period. The aggregated channel throughput ($\mathcal{S}$) of the network, defined

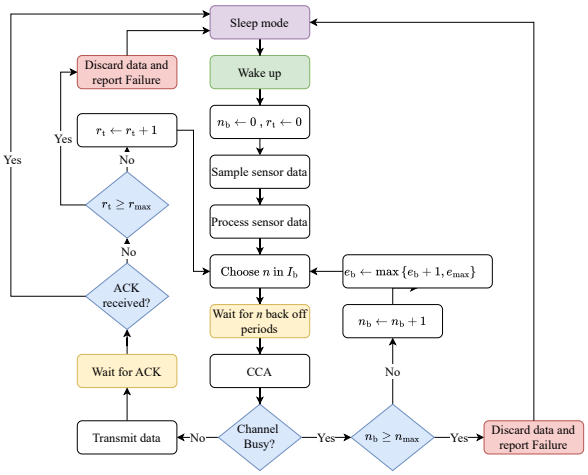

Fig. 6. The basic SN operation, including data collection and medium access control.

as the fraction of time in which the RF channel successfully transmits data [30] is given as:

$$\mathcal{S} = \frac{N_{SN} \cdot P_{success} \cdot L_P}{T_c} \tag{9}$$

where L_P is the packet length in timeslots, $P_{success}$ is the probability a node successfully transmits within a cycle and T_c represents the total number of timeslots within a cycle during which at least one node is active. This includes all associated activities such as backoff periods, CCAs, transmission attempts and ACK durations (L_{ACK}). Both $P_{success}$ and T_c depend on N_{SN}. For $L_p = 2$ (20 bytes) and $L_{ACK} = 1$ (10 bytes), the average throughput is shown in Figure 7, as we vary the number of SNs up to 40 and run the algorithm for 200000 iterations. For simulation purposes, we consider that every node exits the sleep mode at a timeslot randomly selected inside the interval $[0, T)$.

Note that T is very large compared to the duration during which a node is typically active, implying a small probability of collision and a large probability that a node will successfully transmit the packet on the first try. Consequently, the decrease in $\mathcal{S}$ remains minimal as the number of nodes increases. This reduction in $\mathcal{S}$ results from a higher probability of packet collisions and increased probability that the SNs will sense the channel as busy when performing CCA. The average backoff duration

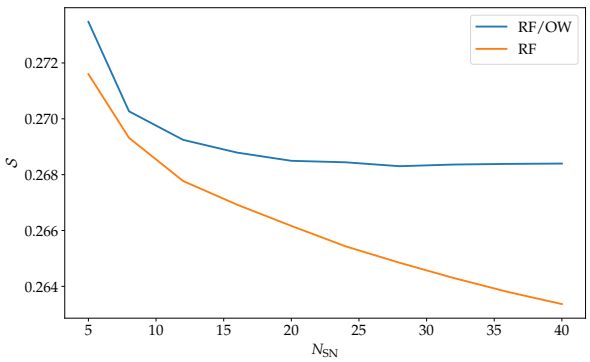

Fig. 7. Throughput of modified unslotted CSMA/CA protocol for the RF/OW and purely RF systems.

per transmission per node increases marginally from 3.5 to 3.8 backoff periods as N_{SN} increases from 5 to 40. It is important to note that the value of $\mathcal{S} \approx 0.27$ arises from the inclusion of time spent in backoff periods, ACK transmissions and other overheads in the denominator of Eq. 9. For comparison, we also plot the performance of a pure RF system, which uses RF for ACK transmissions. The performance declines faster as N_{SN} increases, as shown in Figure 7. This configuration results in a busier channel, leading to longer backoff periods and reduced overall efficiency.

D. PV panel model

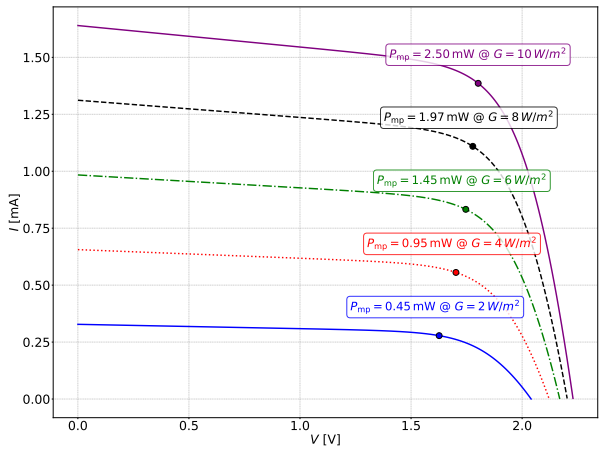

Fig. 8. Simulated I-V curves for indoor irradiance levels.

The five-parameter model [31] is used for accurately describing the electrical characteristics of PV panels used for EH at the SNs. The parameters involved are the photocurrent I_{ph}, reverse diode saturation current I_0, series and parallel resistors R_s and R_{sh}, respectively, and the ideality factor of the diode η. Using this model, we obtain the following I-V curve for the PV:

$$I = I_{ph} - I_0 \left[\exp\left(\frac{q(V + IR_s)}{N_{cell}\eta k_B T_K}\right) - 1\right] - \frac{V + IR_s}{R_{sh}} \tag{10}$$

Manufacturers typically provide the open-circuit voltage V_{oc}, the short-circuit current I_{sc} as well as the maximum power voltage and current points, V_{mp} and I_{mp}, respectively, at a reference irradiance level G_0. To derive the I-V curve, we use the approach of [32], assuming that both R_{sh} and R_s are inversely proportional to the irradiance G [33], while V_{oc} varies logarithmically with G, as given by:

$$V_{oc}(G) = V_{oc}(G_0) + nN_{cell}\frac{k_B T_K}{q_e} \ln\left(\frac{G}{G_0}\right) \tag{11}$$

where N_{cell} is the number of cells connected in series, while G_0 is a reference irradiance under standard testing conditions, k_B is Boltzmann's constant and q_e is electron charge, and T_K is the temperature in Kelvins, assumed to be 300 K. We also assume $I_{sc}(G) = I_{sc}(G_0)G/G_0$ [33]. Once the five parameters have been extracted, the output I-V characteristic can be obtained by numerically solving Eq. 10 over the voltage range from 0 to $V_{oc}(G_0)$.

We have implemented the method of [32] as part of our `Python` module, and the results obtained are illustrated in Table 1, along with the reference parameters at $G_0 = 1\text{kW/m}^2$ taken from the mono-crystalline Voltaic P121 PV cell [23]. The

simulated I-V characteristics for different levels of irradiance in indoor conditions can be seen in Figure 8.

E. Battery charging circuit

To provide charging current with a constant voltage to the battery of the SNs and to ensure the PVs operate at the maximum power point, an EH power manager integrated circuit (IC) can be used. These are low-power buck or buck-boost converters using maximum power point tracking (MPPT) controllers to maximize the power extracted from the PVs. In our work, the SPV1050 IC is assumed to operate in buck-boost mode. Assuming an ideal MPPT controller, PVs are considered to operate at the maximum power point, as the controller dynamically adjusts their effective load. In this configuration, the converter operates at an efficiency $\eta_{\text{bb}} \cong 80\%$ and the output power of the converter $P_{\text{bb}} = \eta_{\text{bb}} P_{\text{mp}} = \eta_{\text{bb}} \eta_{\text{PV}} P_{\text{TOT}}$, where η_{PV} is the efficiency of the PV panel and P_{TOT} is the incident optical power to the PV panel. The output voltage is set at 4.2 V, which corresponds to the charging voltage of a typical 250 mAh coin cell battery, while the IC limits the output current to ≤ 70 mA. A maximum of $P_{\text{bb}}^{\text{max}} = \max\{P_{\text{bb}}\} = 294$ mW can be used for charging purposes. At a given time duration τ, the energy harvested $\mathcal{E}_{\text{h}}(\tau) = P_{\text{bb}}\tau$. The energy required to fully charge the battery $\mathcal{E}_{\text{batt}} = Q_{\text{batt}} V_{\text{batt}}$, where Q_{batt} is the battery charge capacity. In our calculations, we also assume a self-discharge current $I_{\text{SD}} = 1\ \mu$A.

3. ENERGY CONSUMPTION AND HARVESTING

A. Energy Consumption

To estimate the energy consumption at the SN, we need to consider the supply current $I(t)$ drawn from the battery at each stage of the SN cycle. In the following, we adopt the specifications of the CC1352P7 board [21]. Figure 9 illustrates a representative current cycle, which is intended for illustrative purposes only and is not drawn to scale. Corresponding typical current values are provided in Table 1. During the sleep mode, the MCU requires limited supply current to support real-time clocking of the order of a few microamps. There is a short wake-up stage lasting $t_{\text{WU}} = 20\mu$s where the MCU is initialized. The next stage involves reading the data from the sensors, where the MCU is in the active state, which requires a supply current of I_{ACT}. During sensor read-out, the sensors need to be powered, each drawing a supply current of I_i. The ADC module is also active and requires a supply current of I_{ADC}. Hence, the total supply current during read-out is given as:

$$I_{\text{SENS}} = I_{\text{ACT}} + \sum_{i=1}^{N} I_i + I_{\text{ADC}} \tag{12}$$

where N is the number of sensors. We consider an MQ-2 gas, a DHT11 temperature and a TSL2561 luminosity sensor, with current values of $I_1 = 0.16$ A, $I_2 = 0.2$ mA and $I_3 = 0.5$ mA respectively.

The sensing stage duration $t_{\text{SENS}} = n_{\text{S}}/f_{\text{S}}$ depends on the sampling frequency f_{S} of the MCU, and the number of samples n_{S} required. For CC1352P7 $f_{\text{S}} = 200$kHz and we assume 4 samples per sensor, totaling $n_{\text{S}} = 12$ samples. The processing stage phase time is $t_{\text{PROC}} = n_{\text{C}}/f_{\text{MCU}}$, where n_{C} is the number of MCU cycles required to process the data and the clock frequency f_{MCU}. We assume n_{C}=5000 cycles, $f_{\text{MCU}} = 48$ MHz and a supply current equal to the active MCU current I_{ACT}. During the backoff states that follow the supply current is also equal to

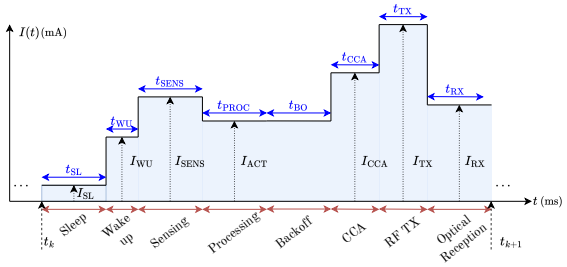

Fig. 9. Variation of the supply current $I(t)$ during a typical SN cycle. SL: sleep (standby) mode, WU: wake up stage, SENS: sensor read-out, PROC: data processing, BO: backoff cycle, CCA: clear channel assessment, Tx: transmission of data using RF, RX: ACK reception using the optical receiver. The area under the curve, highlighted in light blue color corresponds to the charge Q_k drawn from the battery.

I_{ACT}. The first backoff state lasts $t_{\text{BO}} = nT_{\text{b}}$, $n \in [0, 2^{e_{\text{min}}})$ and is followed by the CCA period $t_{\text{CCA}} = 0.3T_{\text{b}}$. If the channel is busy (not shown in Figure 9), then the SN may reenter the backoff state under the provisions of the MAC protocol as in Figure 6. However, if the channel is clear, then the SN transmits data through the RF channel. The supply current I_{TX} drawn depends on the RF transceiver specs. For CC1352P7, it is specified to be 4 mA for P_{t}= -20 dBm and 10 mA at P_{t} = +5 dBm [21]. Considering a linear interpolation yields the following relation between I_{TX} and P_{t}:

$$I_{\text{TX}} \approx 0.24 P_{\text{t}} + 8.8 \tag{13}$$

After the successful transmission of data, the SN switches on its optical receiver and waits for the ACK. At this stage, the supply current is the sum of the I_{ACT} and the bias currents for the TIA and the ADC, I_{TIA} and I_{ADC} respectively, as given by:

$$I_{\text{RX}} = I_{\text{ACT}} + I_{\text{TIA}} + I_{\text{ADC}} \tag{14}$$

If the ACK is not received, the SN may attempt retransmission, jumping back to the backoff state as illustrated in Figure 6. To estimate the energy consumed on the cycle k, we need, first, to estimate the charge drawn from the SN battery, which is given by:

$$Q_k = \int_{t_k}^{t_{k+1}} I(t)\mathrm{d}t \tag{15}$$

where t_k and t_{k+1} are the starting and ending times of cycle k, with $t_{k+1} - t_k = T$. Note that Q_k is the area under the curve $I(t)$, highlighted with light blue color in Figure 9, and can be numerically estimated once stage timings are determined. The energy E_k consumed in the k_{th} cycle is the product of the charge and the supply voltage V_{S}, which is assumed equal to 3 V, $E_k = V_{\text{S}} Q_k$. We should emphasize that utilizing the VLC channel for ACK transmission reduces the average backoff attempts, n_{b} in each node, since the probability of sensing the RF channel idle when performing CCA is greater than in the case where RF is used for sending the ACKs. Therefore, energy consumption for the SN is reduced. Our discrete-event MAC simulation module can be easily applied to estimate the energy consumption over a large number of cycles and to obtain the average energy consumption per cycle, i.e., $\mathcal{E} = \mathbb{E}\{E_k\}$. The average daily consumption $\mathcal{E}_{\text{day}} = \frac{3600\times 24}{T} \cdot \mathcal{E}$, where T is assumed to be measured in seconds.

B. PV performance in indoor conditions

To calculate the incident optical power at the PV, we use the approach of Subsection 2.A, incorporating an additional absorption coefficient $\alpha(\theta)$, which depends on the incidence angle θ due to the nature of the active layer absorption. The absorption coefficient $\alpha(\theta)$ is taken from [24]. This results in a modified LOS gain, $h' = h(\mathbf{r}_S, \mathbf{r}_R)\alpha(\theta)$ that is used instead of h in Eq. (3), in which, we set FOV $= 2\pi$, as $\alpha(\theta)$ includes the relationship between the angle of incidence and light absorption. Similar to the PD, the PV is described by a responsivity spectrum $R_{PV}(\lambda)$.

The incident power at the PV comes from the ambient sunlight through the windows and lamps within the room. For the latter, we use the spectral mismatch factor F_{LAMP} [34], to account for the difference between the lamp spectrum $R_S(\lambda)$ and the reference spectrum $\mathcal{S}(\lambda)$ used in the PV's responsivity measurements:

$$F_{LAMP} = \frac{\int_0^{+\infty} R_S(\lambda)\mathcal{R}_{PV}(\lambda)\mathrm{d}\lambda}{\int_0^{+\infty} \mathcal{S}(\lambda)\mathcal{R}_{PV}(\lambda)\mathrm{d}\lambda} \frac{\int_0^{+\infty} \mathcal{S}(\lambda)\mathrm{d}\lambda}{\int_0^{+\infty} R_S(\lambda)\mathrm{d}\lambda} \quad (16)$$

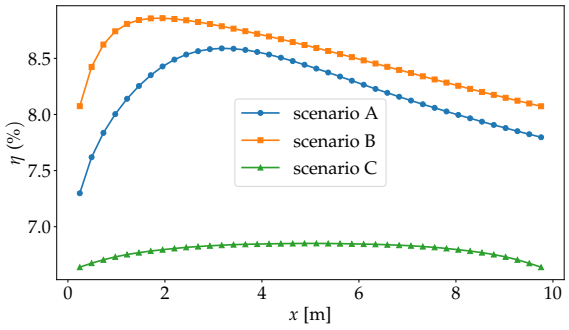

Fig. 10. Simulated efficiency of the PV panels in the diagonal.

A similar factor F_{SUN} can be estimated for sunlight by replacing $R_S(\lambda)$ with $s_q(\lambda)$. However, the reference spectrum closely resembles the sunlight spectrum, i.e., $\mathcal{S}(\lambda) \approx s_q(\lambda)$, and hence $F_{SUN} \approx 1$ and $F_{LAMP} \approx 1.17$. Applying the same approach as in Subsection 2.A, we calculate the total lamp and sun-induced optical power at the PV panel P_{LAMP} and P_{SUN}, respectively. The irradiance is written as:

$$G = \frac{1}{A_{PV}}(P_{SUN} + F_{LAMP}P_{LAMP}) \quad (17)$$

where A_{PV} is the PV area. In our estimations, we have used the spectral response $\mathcal{R}_{PV}$ of the P121 PV cell, which we fitted with a 7^{th} order polynomial with respect to λ, as in Eq. (18), which holds for 300 nm $< \lambda <$ 1200 nm. Outside this range, $\mathcal{R}_{PV}(\lambda) = 0$. The coefficients a_i are listed in Table 1.

$$\mathcal{R}_{PV}(\lambda) = \sum_{i=0}^{7} a_i \cdot \lambda^i \quad (18)$$

Figure 10 shows the efficiency $\eta_{PV} = P_{mp}/P_{TOT}$ of the PV, with $P_{mp} = I_{mp}V_{mp}$ being the maximum power point. The efficiency is estimated along the floor diagonal for the three scenarios. These values are in agreement with typical efficiency measurements in indoor environments [35]. As expected, the efficiency of the Si PV panel significantly decreases under lower irradiance levels, as V_{oc} varies logarithmically with irradiance. However, in the next sections we demonstrate that it is still possible to harvest a considerable amount of energy.

C. Panel orientation

In PV applications, one should pay close attention to the orientation angles, tilt (θ) and azimuth (ϕ) to maximize energy harvesting. For simulation purposes, we assume a near-optimal orientation obtained by a metaheuristic optimization algorithm, and more specifically, the global best particle swarm optimization in a star topology method [36]. This is readily available in the `Pyswarms` module. The cost function was taken as $1/G(\theta, \phi)$. The cognitive parameter was set to 0.5, the social parameter to 0.3 and the inertia weight to 0.8. A swarm size of 20 particles was chosen and the algorithm was executed for 20 iterations to identify the optimal solution. Further increases in the number of particles or iterations did not yield any improvement in the results. Three instances of the problem are considered: one for each scenario. The output power from the PV using the found near-optimal orientation and the naive orientation for the three scenarios can be seen in Figure 11.

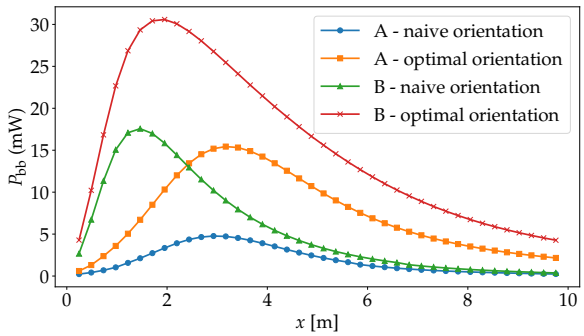

(a) Output power from the PVs in scenarios A and B.

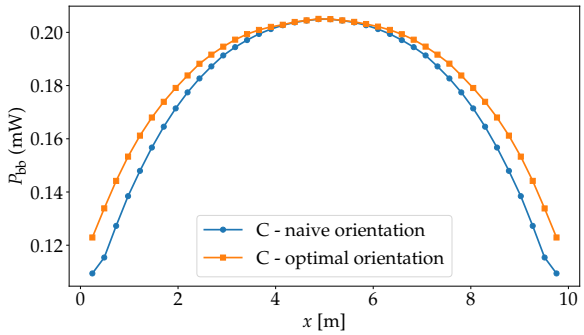

(b) Output power from the PVs in scenario C.

Fig. 11. Output power from the PV panels with naive and optimized orientation.

For the naive orientation, we assume that the PV panels are oriented parallel to the floor plane, facing upwards. In the presence of sunlight, it is best to orient the PV panels toward the window, as the energy available from sunlight is 1-3 orders of magnitude greater than that from the LEDs. In the absence of sunlight, near the center of the room, the optimal orientation coincides with the naive orientation due to the nearly uniform optical power distribution. However, near the walls of the room, minor adjustments may be needed to ensure the PV panels harvest energy from a greater number of ceiling-mounted LEDs.

D. SN energy performance

In this section, we apply the model presented in the previous sections to estimate the EH performance. The simulation parameters for the WSN configuration are listed in Table 1. We first estimate the SN battery lifetime T_{batt} without EH. Figure 12a shows the values of T_{batt}, for an SN placed at various positions on the floor, assuming $N = 20$ nodes in the network and an SN cycle period of $T = 1$ s. A typical 3 V 250 mAh non-rechargeable battery is assumed. The estimated lifetime ranges from 440 to 458 days depending on the SN position, indicating that battery replacements must take place for all nodes within the second year of operation. The worst daily energy consumption is $\mathcal{E}_{\text{day}} \approx 7.55$ J, obtained at the corners of the room. We should note that the optical SN receiver draws $I_{\text{RX}} = 4.1$ mA at the ACK stage compared to 6.4 mA of a purely RF receiver as specified in the CC1352P7 datasheet [21]. As a result, for a purely RF configuration with the same specs, and taking also into account the pure RF MAC protocol, the battery life ranges from 421 to 439 days.

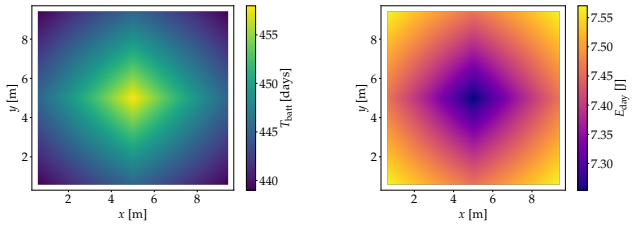

Fig. 12. (a) Battery life estimation, and (b) energy dissipated in a day by the SNs.

When EH is used at the SN, the goal is to ensure there is no energy deficit by setting the consumed energy equal to the harvested energy on a daily basis, i.e., $\mathcal{E}_{\text{day}} = \mathcal{E}_{\text{h}}(\tau) = P_{\text{bb}}\tau$, where τ is the interval in which harvesting takes place within a day. Figure 13 depicts the energy harvested $\mathcal{E}_{\text{h}}(\tau)$ for scenarios A, B, and C, for $\tau = 1$ h. In the first case, we deduce that the harvested energy is sufficient to compensate for the worst case energy dissipation ($\mathcal{E}_{\text{day}} \approx 7.55$ J) at the SN in the majority of possible room positions. There are only 1.2% SN positions, typically located near the room corners, where the time required to fully recharge is larger than 1 hour. In the second case, all nodes require less than half an hour to fully compensate for their energy dissipation. Therefore, installing smaller PV panels should be considered to reduce overall costs. The worst case power consumption and EH results can be seen in Table 1.

In the absence of sunlight, shown in Figure 13c, the harvested power is significantly lower, ranging from 0.45 J/h to 0.7 J/h and energy deficits remain even within an 8 h time period when lighting lamps are switched on. In this case, it is interesting to estimate the required increase in PV cell area A_{PV} to fully compensate for the daily energy dissipation within $\tau = 8$ h, determined by:

$$A_{\text{PV}} = \frac{\mathcal{E}_{\text{day}}}{\eta_{\text{bb}}\eta_{\text{PV}}G\tau} \tag{19}$$

Figure 14 illustrates the values of A_{PV} obtained in this manner. A PV panel with similar efficiency and proper active area can be used. An example is the P124 panel from Voltaic with an effective area of ≈ 75 cm^2.

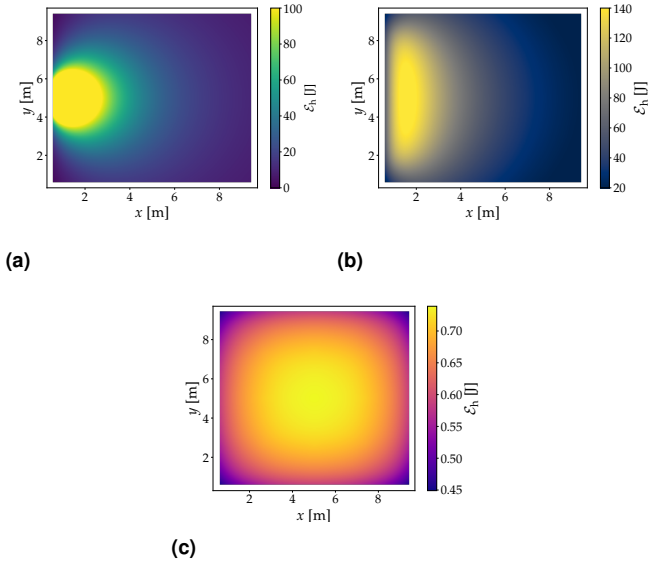

Fig. 13. Harvested power from the P121 PV panel per hour in: (a) scenario A, (b) scenario B, and (c) scenario C.

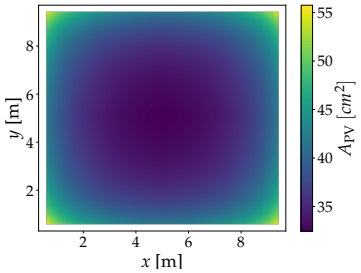

Fig. 14. Required active area of the PV for scenario C.

4. CONCLUSIONS AND OUTLOOK

We have conducted a numerical analysis of an EH-OWRF WSN, where sensory data is transmitted via the RF channel, while ACKs are communicated through the VLC channel. This approach alleviates RF spectrum congestion by offloading traffic to the VLC channel, enhances energy efficiency at the master node since LEDs are reused for data transmission, and reduces power consumption at the sensor node receiver during the ACK phase. Our simulations employed realistic modeling of various communication subsystems, medium access control mechanisms, and energy harvesting processes at both sensor and master nodes. The results highlighted the substantial potential of EH-OWRF technology for IoT and 6G, particularly in terms of system self-sustainability. In the scenarios analyzed, we demonstrated that achieving a zero-energy deficit on a daily basis is feasible. With sunlight available, a mere hour of energy harvesting per day suffices. In the absence of sunlight, a zero-energy deficit can still be attained by using larger PV areas, provided that room lighting remains active for at least eight hours per day. These findings underscore the viability of EH-OWRF systems for sustainable, next-generation IoT networks.

Several important research directions remain open for future investigation, including RF interference, system scalability in terms of the number of SNs, limited coverage scenarios, where multiple MNs and/or multi-hop communication strategies must

be used, and dynamic environments with mobile SNs and moving obstacles.

FUNDING

H2022 Marie Sklodowska-Curie Actions Doctoral Networks (OWIN6G, 101119624)

DISCLOSURES

The authors declare no conflicts of interest.

DATA AVAILABILITY

No data were generated or analyzed in the presented research.

REFERENCES

1. Z. Qadir, K. N. Le, N. Saeed, and H. S. Munawar, "Towards 6G Internet of Things: Recent advances, use cases, and open challenges," ICT Express **9**, 296–312 (2023).
2. R. Salama, F. Al-Turjman, D. Bordoloi, and S. P. Yadav, "Wireless sensor networks and green networking for 6G communication-an overview," in *2023 International Conference on Computational Intelligence, Communication Technology and Networking (CICTN),* (IEEE, 2023), pp. 830–834.
3. L. U. Khan, I. Yaqoob, M. Imran, Z. Han, and C. S. Hong, "6G wireless systems: A vision, architectural elements, and future directions," IEEE access **8**, 147029–147044 (2020).
4. Z. Wei, Z. Wang, J. Zhang, Q. Li, J. Zhang, and H. Fu, "Evolution of optical wireless communication for B5G/6G," Prog. Quantum Electron. **83**, 100398 (2022).
5. B. Donmez, R. Mitra, and F. Miramirkhani, "Channel Modeling and Characterization for VLC-Based Medical Body Sensor Networks: Trends and Challenges," IEEE Access **9**, 153401–153419 (2021).
6. V. Jungnickel, P. W. Berenguer, S. M. Mana, M. Hinrichs, S. M. Kouhini, K. L. Bober, and C. Kottke, "LiFi for Industrial Wireless Applications," in *2020 Optical Fiber Communications Conference and Exhibition (OFC),* (2020), pp. 1–3.
7. S. Javed, L. Issaoui, S. Cho, and H. Chun, "Utilization of LED Grow Lights for Optical Wireless Communication-Based RF-Free Smart-Farming System," Sensors **21** (2021).
8. M. Uysal, Z. Ghassemlooy, A. Bekkali, A. Kadri, and H. Menouar, "Visible Light Communication for Vehicular Networking: Performance Study of a V2V System Using a Measured Headlamp Beam Pattern Model," IEEE Veh. Technol. Mag. **10**, 45–53 (2015).
9. I. Demirkol, D. Camps-Mur, J. Paradells, M. Combalia, W. Popoola, and H. Haas, "Powering the Internet of Things through Light Communication," IEEE Commun. Mag. **57**, 107–113 (2019).
10. H. Abuella, M. Elamassie, M. Uysal, Z. Xu, E. Serpedin, K. A. Qaraqe, and S. Ekin, "Hybrid rf/vlc systems: A comprehensive survey on network topologies, performance analyses, applications, and future directions," IEEE Access **9**, 160402–160436 (2021).
11. H. Shin, S. Park, L. Kim, J. Kim, T. Kim, Y. Song, and S. Lee, "The future service scenarios of 6G telecommunications technology," Telecommun. Policy **48**, 102678 (2024).
12. A. Aslanidis, "EH_RFOW_IoT," https://github.com/AAslan94/EH-RFOW_IoT (2025). Accessed: 2024-04-01.
13. D. Iturralde, J. Guaña-Moya, P. P. Játiva, I. Sánchez, M. Ijaz, A. Dehghan Firoozabadi, and D. Zabala-Blanco, "A New Internet of Things Hybrid VLC/RF System for m-Health in an Underground Mining Industry," Sensors **24** (2024).
14. P. D. Diamantoulakis and G. K. Karagiannidis, "Simultaneous Lightwave Information and Power Transfer (SLIPT) for Indoor IoT Applications," in *GLOBECOM 2017 - 2017 IEEE Global Communications Conference,* (2017), pp. 1–6.
15. T. Tang, L. Shi, Q. Li, and Z. Xiong, "Sustainability-driven resource allocation for slipt-assisted hybrid vlc/rf iot systems," IEEE Wirel. Commun. Lett. **13**, 1765–1769 (2024).
16. v. Khoe Ta, I.-P. Hong, and G. N. Tran, "Slipt-assisted dual-hop vlc/rf with relay selection: Outage probability analysis and optimization," IEEE Access **13**, 41854–41864 (2025).
17. S. Zargari, M. Kolivand, S. Nezamalhosseini, B. Abolhassani, L. Chen, and M. H. Kahaei, "Resource Allocation of Hybrid VLC/RF Systems with Light Energy Harvesting," IEEE Trans. on Green Commun. Netw. **PP**, 1–1 (2021).
18. P. K. Sharma, Y.-S. Jeong, and J. H. Park, "EH-HL: Effective Communication Model by Integrated EH-WSN and Hybrid LiFi/WiFi for IoT," IEEE Internet Things J. **5**, 1719–1726 (2018).
19. G. Pan, H. Lei, Z. Ding, and Q. Ni, "3-D hybrid VLC-RF indoor IoT systems with light energy harvesting," IEEE Trans. on Green Commun. Netw. **3**, 853–865 (2019).
20. T. Kamalakis, Z. Ghassemlooy, S. Zvanovec, and L. N. Alves, "Analysis and simulation of a hybrid visible-light/infrared optical wireless network for IoT applications," J. Opt. Commun. Netw. **14**, 69–78 (2022).
21. T. Instruments, "CC1352P7 SimpleLink™ High-Performance Multi-Band Wireless MCU with Integrated Power Amplifier," (n.d.). Accessed: Nov. 29, 2024.
22. D. O'Rourke, S. Fedor, C. Brennan, and M. Collier, "Reception region characterisation using a 2.4GHz direct sequence spread spectrum radio," in *Proceedings of the 4th Workshop on Embedded Networked Sensors,* (Association for Computing Machinery, New York, NY, USA, 2007), EmNets '07, p. 68–72.
23. V. Systems, "P121 Solar Panel Datasheet," https://voltaicsystems.com/ (n.d.). Accessed: 2024-12-04.
24. C. A. Reynaud, R. Clerc, P. B. Lechêne, M. Hébert, A. Cazier, and A. C. Arias, "Evaluation of indoor photovoltaic power production under directional and diffuse lighting conditions," Sol. Energy Mater. Sol. Cells **200**, 110010 (2019).
25. T. Kamalakis, Z. Ghassemlooy, S. Zvanovec, L. N. Alves, and M. Khalighi, "Optimization and design of a diffuse optical wireless sensor network," Appl. Opt. **61**, 6599–6608 (2022).
26. N. R. E. L. (NREL), "Reference Air Mass 1.5 Spectra," (2024). Accessed: 2024-11-29.
27. C. H. Yeh, C. W. Chow, H. Y. Chen, J. Chen, and Y. L. Liu, "Adaptive 84.44–190 mbit/s phosphor-led wireless communication utilizing no blue filter at practical transmission distance," Opt. Express **22**, 9783–9788 (2014).
28. "IEEE Standard for Low-Rate Wireless Networks," IEEE Std 802.15.4-2020 (Revision IEEE Std 802.15.4-2015) pp. 1–800 (2020).
29. S. Lanzisera and K. S. J. Pister, "Theoretical and Practical Limits to Sensitivity in IEEE 802.15.4 Receivers," in *2007 14th IEEE International Conference on Electronics, Circuits and Systems,* (2007), pp. 1344–1347.
30. I. Ramachandran, A. K. Das, and S. Roy, "Analysis of the contention access period of IEEE 802.15.4 MAC," ACM Trans. Sen. Netw. **3**, 4–es (2007).
31. S. Bader, X. Ma, and B. Oelmann, "One-diode photovoltaic model parameters at indoor illumination levels – A comparison," Sol. Energy **180**, 707–716 (2019).
32. V. Stornelli, M. Muttillo, T. de Rubeis, and I. Nardi, "A New Simplified Five-Parameter Estimation Method for Single-Diode Model of Photovoltaic Panels," Energies **12** (2019).
33. V. Lo Brano, A. Orioli, C. Giuseppina, and A. Di Gangi, "An improved five-parameter model for photovoltaic modules," Sol. Energy Mater. Sol. Cells **94**, 1358–1370 (2010).
34. C. K. Kim, H.-G. Kim, Y.-H. Kang, and M. Oh, "Comprehensive Analysis of Spectral Mismatch Factor for Solar Cells Based on In Situ Observation of Aerosol Optical Depth Spectra and Solar Spectral Irradiance in Korea," Int. J. Energy Res. **2023**, 2617427 (2023).
35. G. Apostolou, A. Reinders, and M. Verwaal, "Comparison of the indoor performance of 12 commercial PV products by a simple model," Energy Sci. & Eng. **4**, 69–85 (2016).
36. J. Kennedy and R. C. Eberhart, "Particle swarm optimization," in *Proceedings of the IEEE International Conference on Neural Networks,* (IEEE, 1995), pp. 1942–1948.